In Vivo Measurement of 3-D Skeletal Kinematics from Sequences of Biplane Radiographs: Application to Knee Kinematics

Byoung-moon You, Pepe Siy, William Anderst, and Scott Tashman*

***Abstract*—Current noninvasive or minimally invasive methods for evaluating *in vivo* knee kinematics are inadequate for accurate determination of dynamic joint function due to limited accuracy and/or insufficient sampling rates. A three-dimensional (3-D) model-based method is presented to estimate skeletal motion of the knee from high-speed sequences of biplane radiographs. The method implicitly assumes that geometrical features cannot be detected reliably and an exact segmentation of bone edges is not always feasible. An existing biplane radiograph system was simulated as two separate single-plane radiograph systems. Position and orientation of the underlying bone was determined for each single-plane view by generating projections through a 3-D volumetric model (from computed tomography), and producing an image (digitally reconstructed radiograph) similar (based on texture information and rough edges of bone) to the two–dimensional radiographs. The absolute 3-D pose was determined using known imaging geometry of the biplane radiograph system and a 3-D line intersection method. Results were compared to data of known accuracy, obtained from a previously established bone-implanted marker method. Difference of controlled *in vitro* tests was on the order of 0.5 mm for translation and 1.4° for rotation. A biplane radiograph sequence of a canine hindlimb during treadmill walking was used for *in vivo* testing, with differences on the order of 0.8 mm for translation and 2.5° for rotation.**

***Index Terms*—2-D/3-D image registration, digitally reconstructed radiograph (DRR), high-speed biplane radiographs, *in vivo* measurement, three-dimensional (3-D) model-based motion analysis.**

I. Introduction

THE *in vivo* measurement of dynamic knee kinematics is important for understanding the effects of joint injuries and diseases, and evaluating treatment effectiveness. Static measurement methods cannot accurately reflect loads encountered during typical movements, and often fail to reliably predict outcome [1]. Therefore, treatments aimed at improving knee function should be evaluated using data obtained from dynamic measurement methods. This requires the determination of six degrees of freedom (DOF) pose (position and orientation) of objects to be estimated during dynamic activities.

The most commonly used methods for assessing dynamic movement rely upon skin-mounted or bone-implanted markers. However, external skin-mounted markers are unable to accurately represent motion of the underlying bone due to movement of soft tissue relative to bone [2]–[7]. To overcome the inherent inaccuracy of skin-mounted markers, markers have been mounted on skeletal pins inserted into the underlying bones [7]–[9], or inserted directly into the bones [10], [11] to measure skeletal kinematics. Though these studies provide some of the best available quantitative data during movement, requirement of skeletal pins or radiopaque markers has limited application for human studies.

Previously, texture-mapped two-dimensional (2-D) models have been used for tracking the human motion in the sagittal plane [12]. In [12], human motion was captured by a video camera and a standard human geometric model was posed on the manually segmented joint positions. The texture pattern of the body image was mapped into the geometric model, and template matching was applied for obtaining the best-matched position between the texture-mapped model and the image. This approach does not appear to be sufficiently accurate for in-depth kinematics analysis due to movements of soft tissue.

Existing three-dimensional (3-D) techniques, such as computed tomography (CT) and magnetic resonance imaging (MRI), allow assessing movements of the underlying bone directly [13]–[15]. However, CT/MRI are not yet capable of achieving high frame rates required for estimating dynamic function. In addition, the restrictions imposed by the imaging environment (typically a small-diameter cylindrical space) prevent full-motion kinematics measurement.

The assumptions and limitations of existing methods described above have impeded accurate measurement of human kinematics under dynamic conditions. These limitations may be overcome by fluoroscopic/radiographic imaging, which enables direct visualization of bone.

Spine position and orientation have been determined using a pattern intensity or gradient-based registration between projections through 3-D CT data and 2-D fluoroscopic images [16], [17]. However, the method was described using high-quality static phantom images and has not been applied to high-speed *in vivo* motion images, which are generally noisy and lower resolution, and may be contaminated with motion artifacts.

A few researchers [18]–[21] have applied image-processing techniques for assessing motion of total knee arthroplasty

Manuscript received October 31, 2000; revised February 28, 2001. This work was supported by a grant from the Whitaker Foundation. The Associate Editor responsible for coordinating the review of this paper and recommending its publication was D. Hawkes. *Asterisk indicates corresponding author.*

B. You and P. Siy are with the Department of Electrical and Computer Engineering, Wayne State University, Detroit, MI 48202 USA.

W. Anderst is with the Motion Analysis Laboratory, Bone and Joint Center, Henry Ford Health System, Detroit, MI 48202 USA.

*S. Tashman are with the Motion Analysis Laboratory, Bone and Joint Center, Henry Ford Health System, Detroit, MI 48202 USA (e-mail: tashman@bjc.hfh.edu).

Publisher Item Identifier S 0278-0062(01)04408-1.

(TKA) components from fluoroscopic images. These studies used known edge (and silhouette) information of the metal components to calculate the similarity between digitally reconstructed radiographs (DRRs) and actual fluoroscopic images. This approach works reasonably well because of the high contrast, well-defined edges created by the dense metal components. However, this method can only be used to study individuals who have undergone joint replacement surgery. Similarly detailed edge information is generally not available from the underlying bone in high-speed radiographic images.

Radiographic images result from a combination of the extent of absorption of both bone and soft tissues. Lower extremity bones have smooth, rounded contours and are covered by varying amounts of soft tissue. Thus, edge information may not represent the exact boundary of the bone, and often cannot be extracted at all from the radiographic images if soft tissues are thick enough. Rapid (up to 2 m/s) bone movement encountered during typical dynamic studies causes significant motion blur at standard video rates, further obscuring edge detail and impairing tracking accuracy. Though available pulsed fluoroscopy systems can reduce blur, typical pulse widths still allow considerable movement during the exposure. For example, a bone moving at 2 m/s shifts 10 mm during 5-ms pulsed exposure. Since one of the goals of this project is to obtain submillimeter accuracy, it is desirable to limit motion during frame acquisition to 1 mm or less—this would dictate an exposure time of 500 μs or less. Since pulsed systems are not generally capable of such short exposures (particularly at 250 frames/s), it is necessary to limit exposure duration by electronically shuttering the video camera. This leads to increased radiation exposure to maintain adequate mR/frame and/or reduced image quality due to quantum mottle effects. These problems are further aggravated by the limited resolution and dynamic range of high-speed video cameras (512 $\times$ 512 $\times$ 8-bit pixels or less), relative to modern fluoroscopy systems (1024$\times$ 1024 $\times$ 10- to 12-bit pixels).

Thus, a new approach was needed based on the assumption that it is not always feasible to identify specific features from the bone. The 3-D pose of the bone can instead be determined by similarity matching (based on texture information and rough edges of bone) of DRRs with the 2-D radiographic images, taking advantage of the redundancy available from two-view radiographs.

Methods for acquisition and processing of radiographic image sequences, development of 3-D bone models and determination of 3-D bone pose are described below. A series of *in vitro* and *in vivo* experiments are then presented to evaluate algorithm performance.

II. Materials and Methods

A. Data Acquisition

A high-speed biplane radiograph system (Fig. 1) has been constructed at the Herrick-Davis Motion Analysis Laboratory (Henry Ford Health System, Detroit, MI) for obtaining high-speed (250 frames/s) biplane radiographic image sequences during movement [22]. The system consists of two 150-kVp X-ray generators (Shimadzu model UD150B-10 with

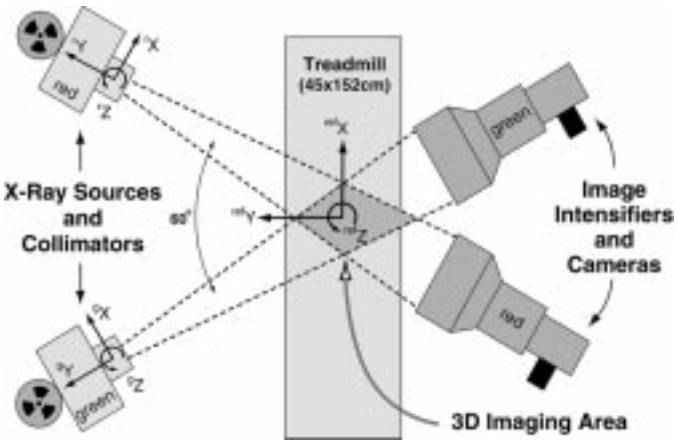

Fig. 1. Configuration of the biplane radiograph system (top view). A global reference coordinate system for the biplane system and two local coordinate systems (single-plane) are shown.

Varian A-262 inserts; 0.6-mm nominal focal spot size), two 30-cm image intensifiers (Shimadzu model AI5765HVP), and two high-speed video cameras (JC Labs HSC-250, 512$\times$ 240 $\times$ 8-bit pixels, 250 frames/s), configured in a custom gantry to enable a variety of motion studies. This system was set up in a configuration commonly used for gait testing (60° interbeam angle, X-ray source to object distance 1.3 m, and object to intensifier distance 0.5 m). This configuration provides a large, open area suitable for either treadmill-assisted or free walking, running, etc. A 567-marker grid was used to correct distortion introduced by the image intensifiers and associated optics [23]. Additionally, a white-field image [acquired from the X-ray system with nothing in the field of view (FOV)] was used to perform a log-based correction for image intensity nonuniformity.

To minimize motion blur during rapid limb movement, the video cameras were electronically shuttered to 1/2000 s for all tests. This limited motion during each video frame exposure to 1 mm or less for bone velocities up to 2 m/s. X-ray beam currents many times greater than typical fluoroscopy were, therefore, necessary to provide sufficient per-frame illumination and reduce noise due to quantum mottle. Tests were typically performed with a continuous 100-mA, 70-kVp protocol, enabling nearly blur-free imaging with per-frame exposure and image quality similar to standard (nonpulsed, 30 frames/s) fluoroscopy. For studies with lower bone velocities, shutter speed and beam current could be proportionally reduced to maintain similar mR/frame exposures, while still limiting bone motion to less than 1 mm during the shutter period. This would maintain the same level of image quality while either reducing subject exposure or enabling longer duration acquisitions. For example, if bone speed does not exceed 1 m/s, shutter speed could be reduced to 1/1000 s and X-ray beam current reduced to 50 mA with no loss of image quality.

For *in vivo* testing, subject radiation exposure was minimized by selecting a specific phase of motion for study (*e.g.*, heelstrike during gait), and precisely synchronizing X-ray exposure to the event of interest (using accelerometers and/or optical sensors and an electronic timer). Additionally, collimators are used to limit beam size to the sensitive area of the image intensifiers,

and restrict primary exposure to the peripheral limb. Experience with this system during walking, running and jumping studies has shown that adequate data can usually be obtained with only 0.5 s X-ray duration, generating estimated entrance exposure of approximately 110 mR/test (times two for biplane studies). A typical knee study might consist of three trials each of two different movement activities, for a total entrance exposure of approximately 1.3 R. This level of radiation exposure is consistent with other diagnostic radiography procedures (e.g., CT scan) and, thus, can generally be justified for diagnostic or research purposes on a case-by-case risk/benefit basis. To maintain radiation exposure within reasonable levels, studies requiring multiple assessments must be intelligently designed to minimize the total number of trials required for each subject. At Henry Ford Health System, research protocols specifying multi-trial testing repeated three times over a two-year period have received Human Rights Committee approval.

A biplane radiographic image sequence of a canine hindlimb available from a prior study [24] was used for development and testing. The right tibia had four bone-implanted radiopaque markers (1.6-mm tantalum beads). This allowed determination of six DOF motion parameters with high accuracy (errors of 0.1 mm for translation and 0.22° for rotation) using the previously developed bone-implanted marker method [22]. A comparison was performed between the bone-implanted marker method and the 3-D model-based method for evaluation of accuracy.

A CT scan of the canine hindlimb was obtained (GE Hi-speed Advantage) to generate a volumetric model for tibia/fibula. Forty-nine 1.0-mm-thick transverse-plane slices (512×512 pixels, 0.488 mm^2 resolution) were acquired from the joint line to 5 cm below from the joint line. Segmentation of the CT-scanned bone was manually performed by thresholding the slices to isolate the bone from soft tissues. Radiopaque marker signatures were identified manually and replaced with the mean values from surrounding voxels to eliminate influences of the markers. The volumetric model was resampled using a bilinear interpolation function to the same resolution as radiographic images acquired with the biplane system.

B. Overview

The 3-D model-based method is based on the assumption that a properly oriented projection through a 3-D volumetric model will produce an image similar to the radiographic images. First, imaging geometry of the biplane radiograph system was determined based on a reference coordinate system [25]. The biplane system was simulated on an SGI workstation (Octane SI with texture option) as two single-plane radiograph systems based on these parameters.

An overview of the process for the single-plane radiograph systems is provided in Fig. 2. The algorithm consists of four major components: volume visualization (model projection), image preprocessing, similarity measurement, and optimization. In the volume visualization step, a 3-D texture-mapping technique is used to project through the 3-D bone model and generate a DRR. During the preprocessing step, a set of image processing algorithms (edge extraction, image enhancement) is applied to extract the coarse edge of the bone. Similarity between the DRR and the radiographic image is determined with a correlation. An optimization algorithm iterates motion parameters until the maximum similarity is obtained. Once six DOF of the center point of the bone model are estimated from each single-plane system, the absolute 3-D position and orientation of the bone in the reference coordinate system are determined using a 3-D line intersection method and the known imaging geometry of the biplane system.

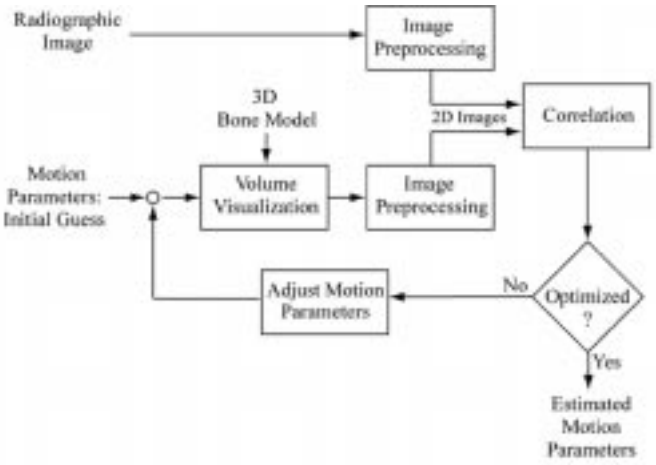

Fig. 2. Overview of the process for measuring the bone position and orientation from the single-plane radiograph system.

C. Determination of Imaging Geometry

Imaging geometry was determined using a 12-marker 3-D calibration cube. The calibration cube was put in the view area of the biplane system, and biplane radiographs were acquired. Positions of each marker were calculated to determine the configuration of the biplane system relative to the global reference coordinate system using the direct linear transformation (DLT) method [25]. Each single-plane system, green and red (denoted by "g" and "r," respectively), of the biplane system was described with its extrinsic and intrinsic parameters. Extrinsic parameters consist of the position and rotation of the X-ray source of the single-plane system in the global reference coordinate system. For the green (red) system, a position vector, ${}^{\mathrm{ref}}P_{\mathrm{gs}}({}^{\mathrm{ref}}P_{\mathrm{rs}})$, a rotation matrix, ${}^{\mathrm{ref}}R^{\mathrm{g}}({}^{\mathrm{ref}}R^{\mathrm{r}})$, were determined from the DLT method. Intrinsic parameters include the principal point and the principal distance of the single-plane system (Fig. 3). The principal point, ${}^{\mathrm{g}}PP({}^{\mathrm{r}}PP)$, is the location in the image plane of the green (red) system, perpendicular to the center of the X-ray beam. The principal distance, ${}^{\mathrm{g}}PD$ $({}^{\mathrm{r}}PD)$, is the distance from the X-ray source to the principal point of the green (red) system. The intrinsic parameters, along with the size and resolution of the radiographic image, were sufficient to accurately simulate two single-plane radiograph systems. The extrinsic parameters were used to reconstruct the biplane system for determining the absolute 3-D pose of the bone in the global reference coordinate system.

D. Volume Visualization

With the geometry of the imaging system known, DRRs can be generated from the 3-D bone model using volume visualization methods [26]–[33]. Perspective (rather than parallel)

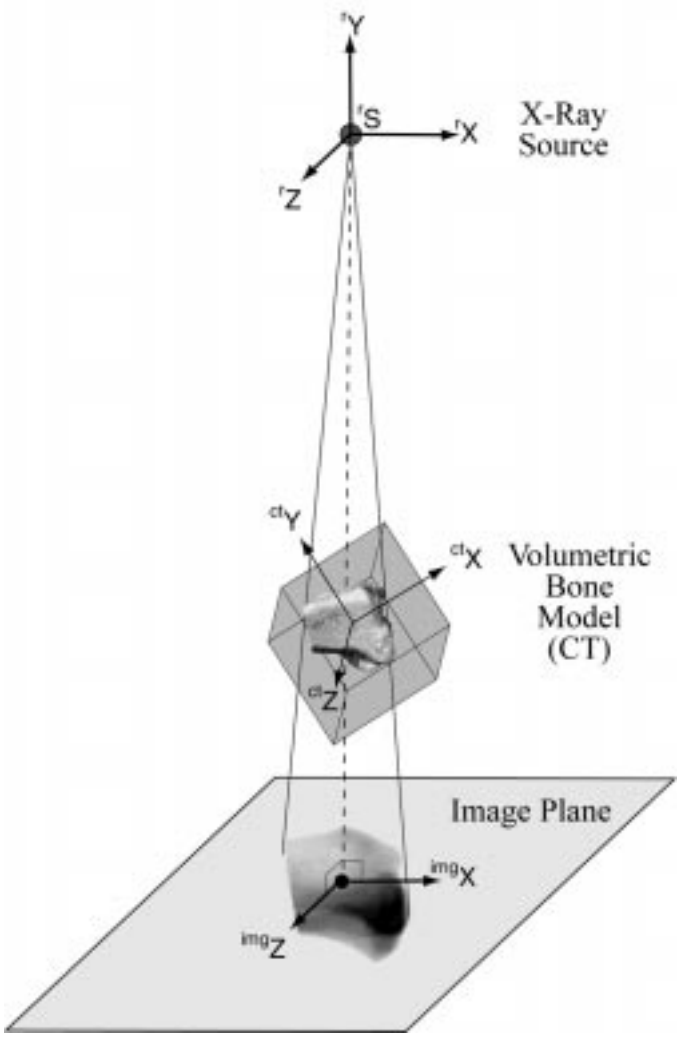

Fig. 3. Imaging geometry of the single-plane radiograph system (red). Principal distance, ${}^{\mathrm{r}}PD$, is from the X-ray source (${}^{\mathrm{r}}S$) to the principal point (${}^{\mathrm{r}}PP$) in the image plane and the principal point is the origin of the image plane. X axis and Z axis of the image plane are parallel to those of the X-ray source.

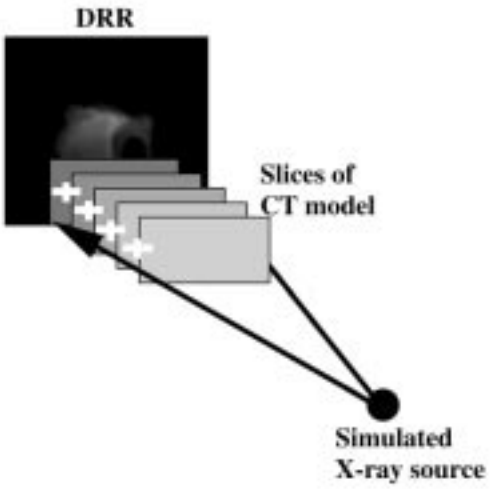

Fig. 4. CT model projection. The CT model is re-sampled with equally spaced planes along the viewing direction and DRR is generated by summing pixel values along projected rays from the X-ray source to the image plane.

Fig. 5. DRR using a 3-D texture-mapped rendering method and a ray-casting method (VTK [27]). (a) Radiographic image of a tibia segment and four radiopaque markers. (b) Three–dimensional texture-mapped rendering method. (c) VTK's ray-casting method. $128\times\ 128\ \times\ 64$ volume data (256 gray level) of the tibia segment were used to generate these images. In the VTK's ray-casting method, scalar opacity transfer function and color transfer function were defined from 0 to 0.005, and 5.0 to 16.0, respectively. The elapsed time to render was about 7 s for the VTK's ray-casting method and 0.3 s for the 3-D texture-mapped rendering method.

projection rendering is required to accurately represent the cone-beam X-ray image formation process. Additive re-projection [26] or ray-casting methods [27], [28] are commonly used for this purpose. However, these methods are computationally intensive, particularly for iterative methods. Restriction of the CT bone model to specific regions [16], [31] and/or precomputing a library of ray integral values have been proposed to accelerate the rendering process [32]. However, for tracking arbitrary orientations of large bones moving through significant volumes, the computational cost of precomputing the required number of rays approaches that of ray-casting.

To significantly reduce rendering time, perspective projections were generated using a hardware-accelerated 3-D texture-mapped volume rendering method [33], implemented using the OpenGL graphics library on an SGI Octane workstation. The entire 3-D model volume data was downloaded into texture memory once. To simulate a desired 3-D orientation, the volume was rotated to orient the bone properly and re-sampled in memory to create equally spaced planes perpendicular to the principal axis of the X-ray beam. Each pixel of the DRR was calculated by summing re-sliced pixels along a ray constructed from the X-ray source to the image plane (Fig. 4). This reduces rendering time by a factor of about 20 (see Section IV), at the cost of a slight reduction in the quality of the resulting DRR (relative to traditional ray-casting), as shown in Fig. 5.

E. Image Preprocessing

Relative to conventional fluoroscopic images commonly used for 2-D/3-D image registration [16], [31], radiographic images obtained from high-speed video cameras are noisy and resolution-limited, complicating the feature-extraction process. This situation is worsened by the inherent irregularity of tissue density and distribution. The combination of these factors can make reliable detection of anatomical features, such as bone edges, difficult or impossible. Thus, it is desirable to extract a feature set using all available information on the bone, rather than only external edges or intensity information. This was accomplished

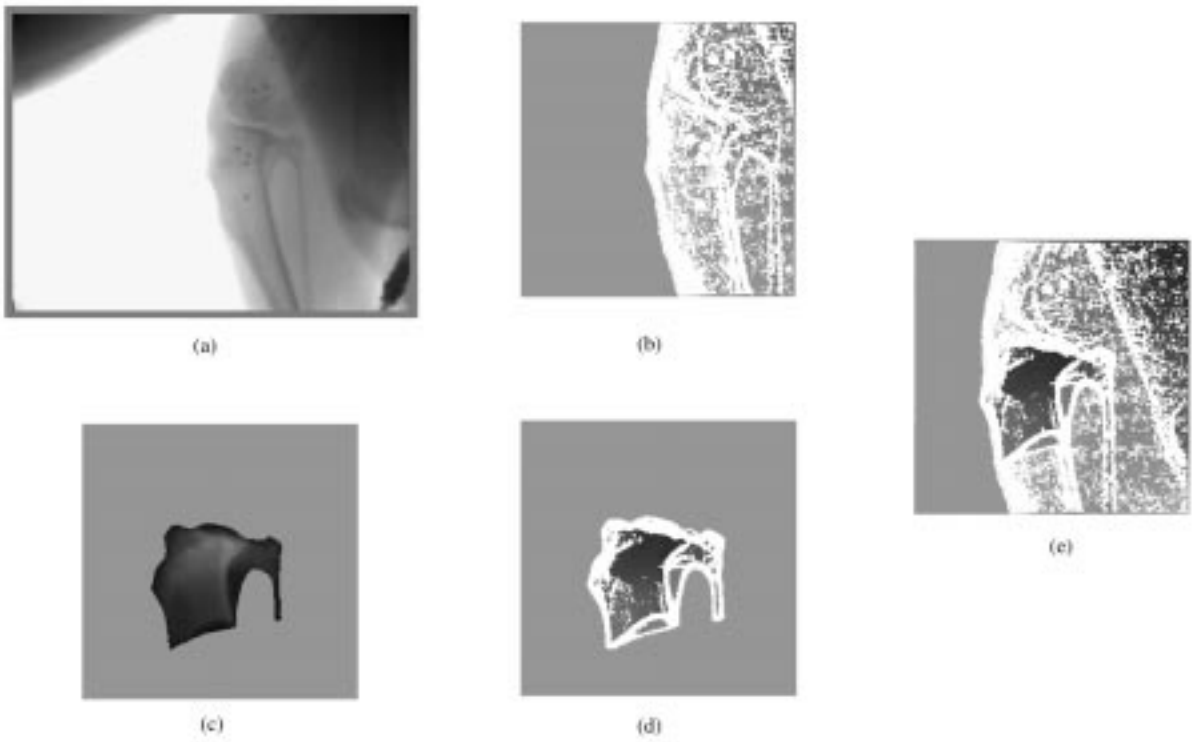

Fig. 6. Preprocessing of a real radiographic image and DRR. (a) An image acquired from the biplane radiograph system. (b) Edge-information added radiographic image (region of interest). (c) DRR generated through the bone model. (d) Inverted and edge-added DRR. (e) Radiographic image overlapped with DRR after the best matching.

by using a combination of edge and intensity information (texture information projected through 3-D volume of bone/model) based on the assumption that even imperfect edge data can serve as useful features for improving matching between the DRR and actual radiographic images.

Both the DRR and the radiographic images are preprocessed prior to matching, to maximize similarity. First, the DRR is inverted and contrast-enhanced using a histogram-equalization algorithm [34], [35] [see Fig. 6(c)]. Then a simple edge algorithm (Sobel edge detector [34], [35]) is applied to extract edges from both DRR and radiographic images. The edge information is then added back to the original images [see Fig. 6(b) and (d)], combining both edge and texture information. The edge information helps to drive the optimization toward the correct solution, improving initial algorithm convergence. However, accuracy with edge information alone is limited due to spurious edges in the radiographic images from the soft tissues, which do not appear in the DRRs. Thus, addition of the intensity/texture information leads to more accurate matching than is possible with edge information alone.

F. Similarity Measurement

To determine optimal position matching, a metric for similarity between two images is required. Pattern intensity [16] and gradient difference methods [17] have been suggested for the DRR and fluoroscopic images. These studies assumed that image quality is high, and that soft tissue structures have a relatively small role in the intensity distribution in fluoroscopic images. Because high-speed radiographs are noisy and contrast-limited and there is a great deal of soft tissue motion during dynamic studies, detectable edges and features in the actual radiographs differ from those in the DRRs. Thus, these assumptions are no longer valid and a different approach was required.

Evaluation of several different correlation strategies suggested that general normalized correlation [34], [35], applied to summed edge/intensity images, is robust even in the presence of these differences between actual radiographs and DRRs. The correlation equation used for this study is

$$V(x,y) = \frac{\sum_{x,y}[r(x,y)-\overline{r_{u,v}}][m(x-u,y-v)-\overline{m}]}{\left\{\sum_{x,y}[r(x,y)-\overline{r_{u,v}}]^2\sum_{x,y}[m(x-u,y-v)-\overline{m}]^2\right\}^{1/2}} \quad (1)$$

where:

$r(x,y)$ radiographic image;
$m(x,y)$ DRR generated from the 3-D CT model;
$\overline{m}$ mean of the DRR;
$\overline{r_{u,v}}$ mean of radiographic image in the region under the DRR.

However, this is computationally intensive, especially if the size of images to be compared is large (as is often the case with medical images). A new Quadtree-based normalized correlation method was employed to reduce search iterations and improve optimization efficiency. A predefined search space of the radiographic image is divided into four quadrants (Fig. 7). The

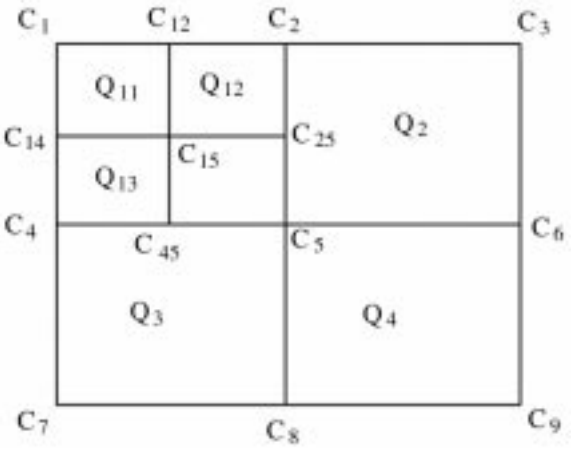

Fig. 7. Quadtree-based correlation. Correlation space is divided into four regions. The region with the best match is subdivided again. This process is repeated until the region size is reduced to 4 × 4 pixels.

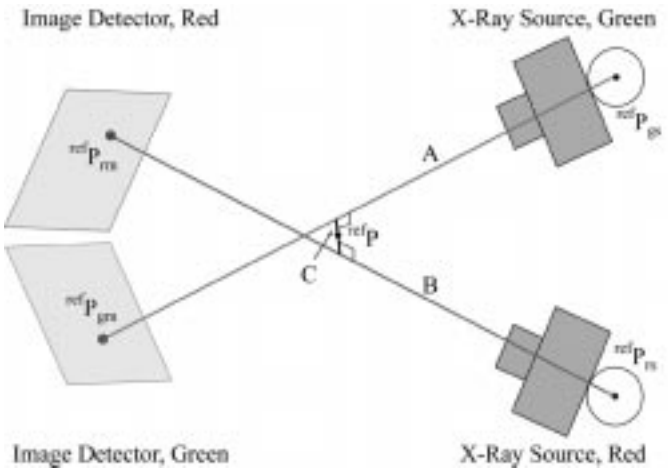

Fig. 8. Determination of 3-D bone position. ${}^{\rm ref}P_{\rm gs}({}^{\rm ref}P_{\rm rs})$ is position of the X-ray source of the green (red) system relative to the reference coordinate system. ${}^{\rm ref}P_{\rm gm}({}^{\rm ref}P_{\rm rm})$ is the best-matching location in the green (red) image plane expressed in the reference coordinate system. The mid-point of the line segment "**C**" is chosen as the optimal 3-D position.

average correlation value (AC_{q1}, AC_{q2}, AC_{q3}, AC_{q4}) of each quadrant (Q_1, Q_2, Q_3, Q_4) is calculated from correlation values of four corner points of the corresponding quadrant (2). The quadrant with the best correlation is further divided for the next step (3). For example, if AC_{q1} is the optimal, AC_{q11}, AC_{q12}, AC_{q13}, and AC_{q14} are calculated. This procedure continues until the size of a quadrant reduces to 4 × 4 pixels. In the final step, all pixels of the optimal quadrant of the radiographic image are correlated with the DRR. The coordinate of the pixel with the best match is chosen as the location of the bone center in the image plane (${}^{\rm ref}P_{\rm gm}$ and ${}^{\rm ref}P_{\rm rm}$, see Fig. 8). The value of the correlation function at this point is used as an indicator of the quality of match for the optimization process described below. For a maximum expected frame-to-frame translation of 20 pixels (40 × 40 pixel search region), the efficiency of the Quadtree algorithm is clearly illustrated. Conventional sequential correlation would require 1600 image multiplications to find the best matching position, whereas the Quadtree-based correlation method requires only 40 multiplications.

At the first iteration

$$\begin{aligned} AC_{q1} &= \frac{c_1 + c_2 + c_4 + c_5}{4}, \quad \text{for quadrant } Q_1 \\ AC_{q2} &= \frac{c_2 + c_3 + c_5 + c_6}{4}, \quad \text{for quadrant } Q_2 \\ AC_{q3} &= \frac{c_4 + c_5 + c_7 + c_8}{4}, \quad \text{for quadrant } Q_3 \\ AC_{q4} &= \frac{c_5 + c_6 + c_8 + c_9}{4}, \quad \text{for quadrant } Q_4. \end{aligned} \tag{2}$$

At the second iteration,

$$\begin{aligned} AC_{q11} &= \frac{c_1 + c_{12} + c_{14} + c_{15}}{4}, \quad \text{for quadrant } Q_{11} \\ AC_{q12} &= \frac{c_{12} + c_2 + c_{15} + c_{25}}{4}, \quad \text{for quadrant } Q_{12} \\ AC_{q13} &= \frac{c_{14} + c_{15} + c_4 + c_{45}}{4}, \quad \text{for quadrant } Q_{13} \\ AC_{q14} &= \frac{c_{15} + c_{25} + c_{45} + c_5}{4}, \quad \text{for quadrant } Q_{14}. \end{aligned} \tag{3}$$

G. Optimization

The downhill Simplex method [36], [37] is used to adjust estimated bone position and orientation until optimal similarity is obtained. The Simplex method requires $N+1$ points as starting points, where N is the number of DOFs of the function being optimized. Then the simplex method travels through the parameter space by reflection and contraction. Estimating 3-D kinematics would typically require simultaneous optimization of all six motion parameters (three positions and three rotations). But, in this study, movements parallel to the image plane (typically less than 20 cm) were considered small relative to the distance from the X-ray source to the bone (approximately 150 cm). Thus the effects of translations parallel to the image plane on the appearance of the projected bone were considered negligible (the validity of this assumption is addressed in the Discussion). The center of the bone model was constrained to move along the principal axis (Fig. 3) and only three rotation parameters and the distance perpendicular to the image plane (out-of-plane position) were controlled by the optimization process to generate DRRs. The remaining two DOF parameters (in-plane position) were directly determined from correlation by finding the best-matching location in the image plane. This reduction of optimization variables from six to four dramatically improved optimization efficiency.

The optimization routine began with five predefined vertices (four DOF plus one, as required for Simplex) as the starting points. An initial guess was determined manually for the first frame or selected as the optimal position of the previous motion frame. The remaining four vertices were selected to span the range of physiologically valid bone orientations. DRRs for each vertex were generated from the 3-D model using the known imaging geometry of a single-plane system and four DOF parameters (three orientation parameters and out-of-plane position parameter) controlled by the optimization process. Then two in-plane position parameters were determined from correlation between the DRRs and the radiographic images. Each reflection or contraction continued to update the three rotation parameters and the distance perpendicular to the image plane, based on the

previous similarity calculations. The optimization routine was terminated when the distance of points moved in that step was fractionally smaller in magnitude than some tolerance.

To check for local minima, the Simplex routine then restarted from the optimized point, and was allowed to converge again. If the new solution differed from the previous solution by more than a specified tolerance (typically, 1° for rotation), the original solution was rejected as a local (nonglobal) minimum, and the routine was restarted from the new optimum point.

H. Three-Dimensional Determination of Position and Orientation

Six motion parameters can be estimated from a single-plane system for each frame. However, the assessment of out-of-plane translations is unreliable with a single-plane system and the accuracy for measuring out-of-plane translations is poor relative to the accuracy for measuring in-plane translations [17], [18]. Thus, only a projection ray passing from the X-ray source, through the center of the bone model, to the best-matching location in the image plane was constructed from each single-plane system. This projection ray was represented as a line segment connecting the X-ray source (the origin of a single-plane system) and the best-matching location in the image plane (${}^{\mathrm{g}}P_{\mathrm{gm}}$ for the green system and ${}^{\mathrm{r}}P_{\mathrm{rm}}$ for the red system).

For simulating the biplane system, Line segments (actually, two end points) estimated from each single-plane system were transformed to the global reference coordinate system based on the information of the position and orientation of single-plane systems relative to the global reference system as follows.

- The position of the X-ray source is the origin of the single-plane system. Its location relative to the global reference coordinate system, ${}^{\mathrm{ref}}P_{\mathrm{gs}}({}^{\mathrm{ref}}P_{\mathrm{rs}})$ for the green (red) system, was already determined from the DLT method.
- ${}^{\mathrm{g}}P_{\mathrm{gm}}({}^{\mathrm{r}}P_{\mathrm{rm}})$ was transformed to the reference coordinate system by a rotation and a translation (4):

$$\begin{aligned} {}^{\mathrm{ref}}P_{\mathrm{gm}} &= {}^{\mathrm{ref}}R^{\mathrm{g\,g}}P_{\mathrm{gm}} + {}^{\mathrm{ref}}P_{\mathrm{gs}} \quad \text{(for the green system)} \\ {}^{\mathrm{ref}}P_{\mathrm{rm}} &= {}^{\mathrm{ref}}R^{\mathrm{r\,r}}P_{\mathrm{rm}} + {}^{\mathrm{ref}}P_{\mathrm{rs}} \quad \text{(for the red system)} \end{aligned} \tag{4}$$

  where ${}^{\mathrm{ref}}R^{\mathrm{g}}({}^{\mathrm{ref}}R^{\mathrm{r}})$ is a 3×3 direction cosine matrix representing the orientation of the green (red) system with respect to the reference coordinate system. ${}^{\mathrm{ref}}P_{\mathrm{gm}}({}^{\mathrm{ref}}P_{\mathrm{rm}})$ is the best-matching location in the image plane of the green (red) system transformed to the reference coordinate system.

For example, two line segments within the reference coordinate system ("**A**" from ${}^{\mathrm{ref}}P_{\mathrm{gs}}$ to ${}^{\mathrm{ref}}P_{\mathrm{gm}}$ and "**B**" from ${}^{\mathrm{ref}}P_{\mathrm{rs}}$ to ${}^{\mathrm{ref}}P_{\mathrm{rm}}$) were constructed, as shown in Fig. 8.

Ideally, the two line segments "**A**" and "**B**" should intersect at a point because they pass through the same point of the bone model. However, these lines generally do not intersect due to errors such as camera calibration, image noise, matching error, etc. To solve this problem, the 3-D position of the bone was determined by finding the midpoint of the shortest line, "**C**", between these two line segments using a 3-D line intersection method [38], [39] (Fig. 8).

Orientation of the bone (α, β, γ) could be determined from the estimated orientation $({}^{\mathrm{ct}}R_{\mathrm{b}})$ of the bone model estimated in each single-plane system assuming body-fixed Y–X–Z rotations [40], [41]

$$\begin{aligned} {}^{\mathrm{ref}}R_{\mathrm{gb}} &= {}^{\mathrm{ref}}R^{\mathrm{g\,g}}R^{\mathrm{ct\ ct}}R_{\mathrm{b}}, \quad \text{for green system} \quad \text{or} \\ {}^{\mathrm{ref}}R_{\mathrm{rb}} &= {}^{\mathrm{ref}}R^{\mathrm{r\ r}}R^{\mathrm{ct\ ct}}R_{\mathrm{b}}, \quad \text{for red system} \end{aligned} \tag{5}$$

where

${}^{\mathrm{ct}}R_{\mathrm{b}}$	constant 3×3 direction cosine matrix of the orientation of the anatomical bone relative to the CT model;
${}^{\mathrm{g}}R^{\mathrm{ct}}({}^{\mathrm{r}}R^{\mathrm{ct}})$	3×3 direction cosine matrix representing the orientation of the CT model with respect to the green (red) system, determined from single-plane optimization;
${}^{\mathrm{ref}}R_{\mathrm{gb}}({}^{\mathrm{ref}}R_{\mathrm{rb}})$	3×3 direction cosine matrix of the bone expressed in the reference coordinate system.

Final 3-D orientation of the bone was determined by averaging the rotation angles obtained from the two single-plane views

$$\begin{aligned} \alpha &= \frac{\alpha_{\mathrm{gm}} + \alpha_{\mathrm{rm}}}{2} \\ \beta &= \frac{\beta_{\mathrm{gm}} + \beta_{\mathrm{rm}}}{2} \\ \gamma &= \frac{\gamma_{\mathrm{gm}} + \gamma_{\mathrm{rm}}}{2} \end{aligned} \tag{6}$$

III. Experiments

Dynamic *in vitro* tests were performed with a canine tibia segment, from which soft tissue was removed. Four tantalum spheres (1.6-mm diameter) were implanted in the bone to enable marker-based tracking. The tibia was held fixed in a vice attached to a computer-controlled stepper motor driven positioning system capable of two-axis linear movement and single-axis rotation (0.006 35 mm/step, 0.02°/step). Three tests were performed: simple translation, simple rotation, and a combination of translation and rotation. In the translation experiment, the tibia segment was positioned vertically (with its long axis perpendicular to the ground) and controlled to move parallel to the ground (in the X–Y plane) in diagonal directions along a 100-mm square. For the rotation experiment, the tibia was rotated ±15° internally/externally about its long (Z) axis. Finally, for combined translation and rotation, the tibia was moved diagonally in the X–Y plane with simultaneous ±10° rotation about the flexion/extension (Y) axis. From each experiment, a sequence of 124 radiographic images was acquired from the biplane radiograph system.

For the first frame of each sequence, the six motion parameters were estimated manually using a window-based user interface to produce DRR that appeared similar to the actual radiographic image. These parameters were used as an initial guess to start the optimization. Fig. 9 illustrates the process that the optimization routine followed to get the best matching from the initial guess. The optimization routine took about 80 iterations for the initial guess and about 60 iterations for tracking the bone

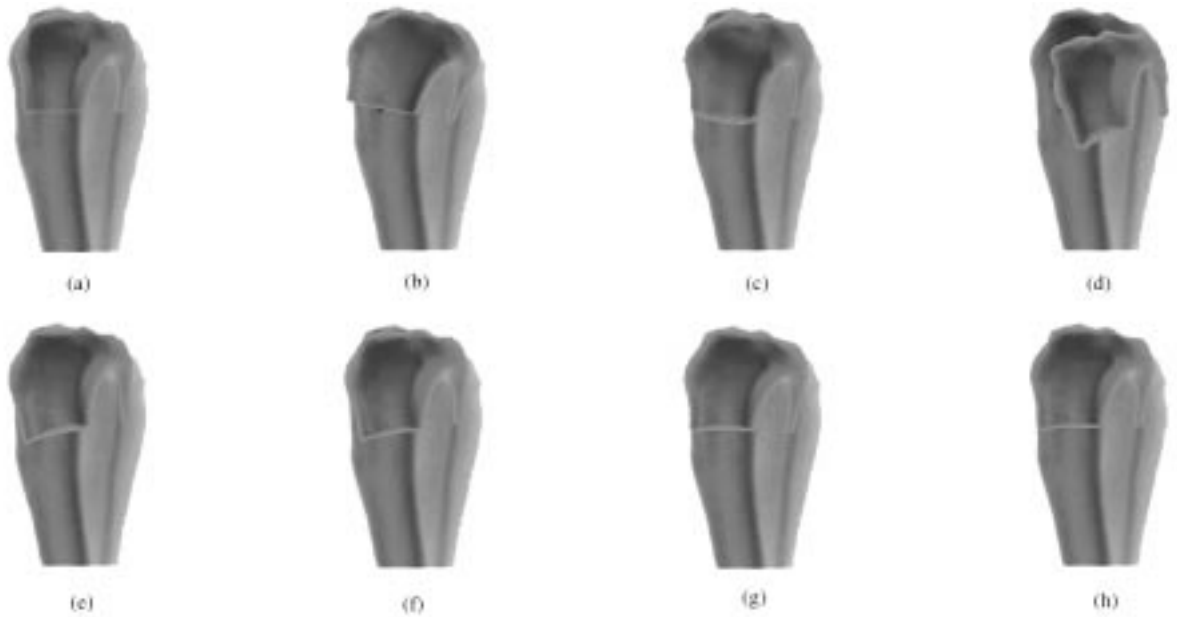

Fig. 9. An example of optimization process. (a) Manual guess. (b)–(e) Predefined vertices spanning range of expected bone motion to initialize the simplex algorithm. (f) 10th iteration. (g) 20th iteration. (h) 45th iteration (optimized).

TABLE I
ROOT-MEAN-SQUARE ERRORS FOR *IN VITRO* AND *IN VIVO* EXPERIMENTS BETWEEN THE 3-D MODEL-BASED METHOD AND THE MARKER-BASED METHOD

	Translation (mm)			Rotation (degrees)		
	X-axis	Y-axis	Z-axis	X-axis	Y-axis	Z-axis
In vitro tests						
XY translation	0.15	0.21	0.18	0.94	0.56	1.34
Z-axis rotation	0.36	0.45	0.22	1.23	1.05	1.65
XY trans., Y rot.	0.12	0.28	0.14	1.16	1.48	1.15
In vivo test	0.25	0.58	0.77	3.86	1.35	2.56

from frame to frame. The average time taken by an iteration, which includes preprocessing of a radiographic image, model projection and the Quadtree-based correlation, was 0.8 s for a $256 \times 256 \times 8$ bit image (SGI Octane, dual 175-MHz processors). The biplane image sequences were also tracked using the marker-based method described in Section II (accuracy for marker tracking: ± 0.1 mm [22]). This marker-based tracking used the same calibration cube and distortion correction images as the 3-D model-based method, providing a common global coordinate system for comparison. For three *in vitro* tests, the root mean square (rms) differences between methods were averaged 0.23 mm for transition and 1.2° for rotation (Table I). The tracking results of the *in vitro* test for combination of translation and rotation are plotted in Fig. 10.

In vivo testing was performed similarly to the *in vitro* study. Biplane radiographic image sequences and limb CT scans were available from an ongoing study of canine knee kinematics. This study utilized implanted tantalum beads (four/bone) for tracking bone motion, thus providing a set of high-accuracy kinematic data for comparison. Biplane radiographs of the right hindlimb were acquired at 250 frames/s during treadmill walking at 1.5 m/s (Fig. 11), using the radiographic protocols described in Section II. Forty continuous frames of a gait sequence were selected with no occlusion between legs. A CT scan of the same limb was acquired and processed to remove tantalum marker signatures. The tibia of the right hindlimb was then tracked using both the 3-D model-based method and the marker-based method, and the results were compared as described for the *in vitro* study (Table I). rms differences between methods were averaged 0.5 mm for transition and 2.6° for rotation.

IV. DISCUSSION

A 3-D model-based method was presented to assess skeletal motion of underlying bone from high-speed sequences of biplane radiographs. The method is based upon optimizing similarity between the radiographic image pairs and DRRs generated by projections through a 3-D bone model (generated from CT). However, the matching between DRRs and actual radiographic images can never be exact. The radiographic images result from a combination of the extent of absorption of both bone and soft tissues, and soft tissues obscure the outmost edges of the underlying bone. In contrast, the exact outmost edges of the bone can be obtained from the CT volume data, from which soft tissues were removed manually. This causes an apparent difference in size between real radiographic images and DRRs (the projected bone looked bigger than the bone in the radiographic images). This difference varies by frame and is difficult to correct. Single-plane implementation of the algorithm resulted in bone position estimates farther away from the X-ray source than the absolute position determined using stereo information or marker-based tracking (Fig. 12). Thus, assessment of movement perpendicular to the image detector was unreliable with a single-plane system. In Fig. 12, bone was estimated 100 mm farther away from the X-ray source of the red system, causing 20-mm errors for X axis and 60-mm errors for Y axis in the reference coordinate system. Similarly large errors parallel to the X-ray beam direction (10 times larger than errors in other axes) have been observed previously in a CT/fluoroscopy

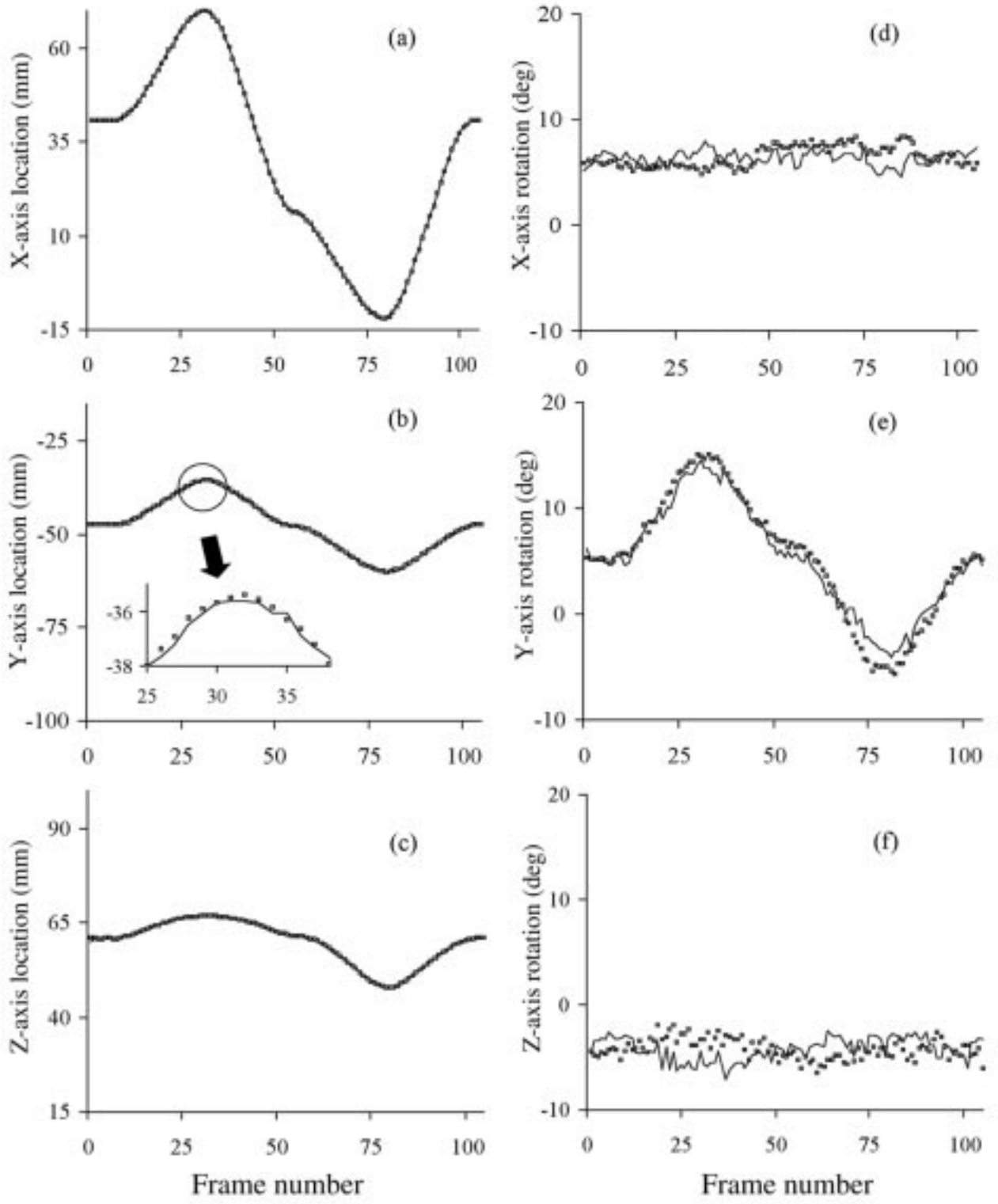

Fig. 10. A comparison between the proposed marker-less method (solid lines) and the marker-based method (circles). (a)–(c) Translations. (d)–(f) Rotations. Translation errors are largest for Y axis, as seen in insert (b). Rotation errors are largest for X axis (d).

registration study of the spine [17]. By combining results from the two views, errors in the beam axis direction are reduced to a level similar to those in the image plane (see Table I; Y axis errors versus X and Z axis errors).

The two line segments connecting each projection source and the coordinates of its projections onto the corresponding image plane should theoretically intersect at a point. But these vectors do not generally cross, due to small errors from various sources (see Fig. 8). During the experiments described above, these two lines typically missed crossing by only about 0.2 mm in each axis. Single-plane systems may be somewhat better for estimating bone rotation, since 3-D rotations calculated separately

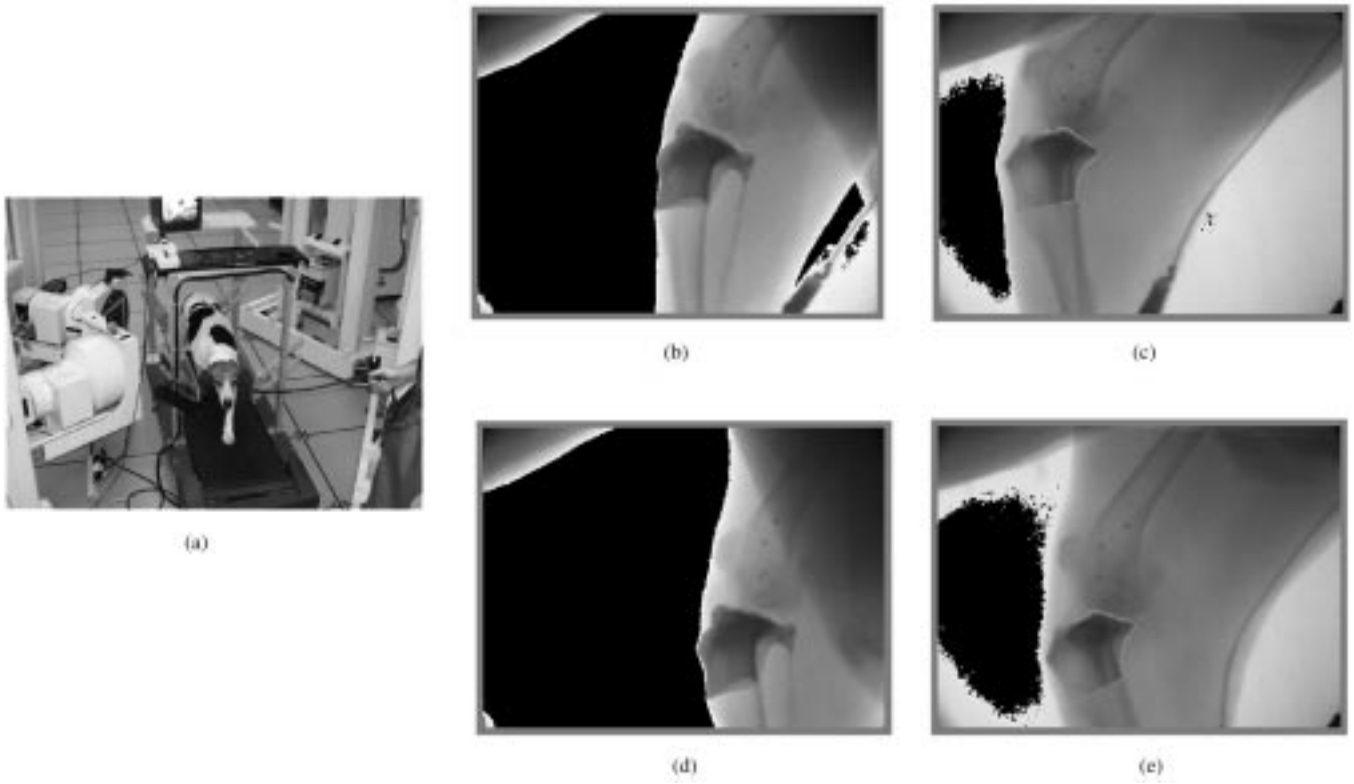

Fig. 11. Images from an *in vivo* experiment. (a) A dog while treadmill walking. (b, c) 40th frame of radiographic images acquired from the green and red system, overlapped with images simulated from CT model. (d, e) 68th frame radiographic images. Background noise was thresholded to zero.

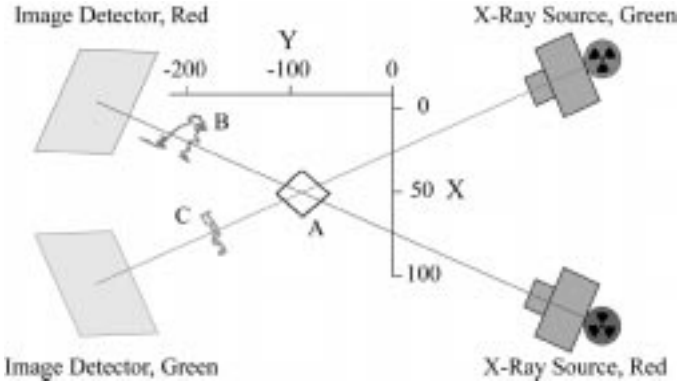

Fig. 12. A XY (transverse) plane movement of an *in vitro* experiment viewed from the top. Bone motion followed a diamond pattern. "**A**" is the path estimated using biplane views (overlapped with an assumed true path determined from the bone-implanted marker method), "**B**" is the path estimated from the red system, and "**C**" is the path estimated from the green system. Single-plane errors along beam direction are large, but resolved when views are combined.

for each system typically differed by only about 0.3° (after the estimated orientation from each single-plane system was transformed to the common reference coordinate system).

When information from both views was combined, the relative differences between model-based tracking and marker-based reference data were approximately 0.5 mm for *in vitro* experiments and 0.8 mm for the *in vivo* experiment for all axes. These errors are similar in magnitude to the effective pixel size of the radiographic images (approximately 0.5 × 0.8 mm with 500 × 240 resolution and 250 × 190 mm FOV). This suggests that radiographic image resolution may be a limiting factor for accuracy, and higher resolution cameras and/or the addition of subpixel matching techniques may improve performance.

Determining the 3-D pose of an object is a six-dimensional (6-D) optimization problem. In this study, the 6-D search space was reduced to four dimensions to greatly improve optimization efficiency. During single-plane optimization, the three orientation parameters are allowed to vary, but the 3-D bone model is allowed to translate only along the principal axis. In-plane translation parameters are subsequently determined from correlation between DRRs and radiographic images. Because of the cone-shaped projection, the shape of the bone in the radiographic image would be expected to change as the bone moves parallel to the image plane; this effect is ignored in the DRR. Since the movement parallel to the image detector is small with respect to the distance from X-ray source to the bone, it is assumed that the effects of this movement on the DRR will cause acceptably small errors.

This assumption was validated by performing a test using DRRs instead of actual radiographs. DRRs were generated with the bone model centered on the principal axis, and also shifted 40 mm along the X axis (parallel to the imaging plane). Single-plane optimizations were performed using these DRR images as inputs. Differences in rotations determined for the two images were 0.1° or less for all three axes. Thus, the contribution of this factor to the total error magnitude (Table I) is likely to be relatively small. This error could be reduced or eliminated in the future by using 6-D optimization during the final stage of the optimization.

Convergence of the optimization algorithm was quite sensitive to the quality of the initial guess for the 6-D motion param-

eters. Experience from these studies suggests that the initial parameters should be within $+/-5^\circ$ for rotation and ten pixels for translation of actual bone pose for reliable convergence on the correct solution. Errors of this magnitude are easily discernable with the graphical user interface provided. Larger errors in the initial guess sometimes led to algorithm failure and/or convergence on a nonoptimal local minima, which was not always corrected by restarting the optimization from the erroneous point. Such failures can be easily detected when results from the biplane views are combined, since the two solutions will be inconsistent. Though generating the initial guess sometimes requires considerable effort on the part of the operator, this effort is only necessary for the first frame of a motion sequence. The fast frame rate limits frame-to-frame motion to less than the tolerances described above, so that each frame result provides an excellent initial guess for the subsequent frame.

Regarding the elapsed time for generating a DRR, the shear-warp based volume rendering method [32] is faster by a factor of almost seven compared to a ray-casting method; transgraph-based rendering method [31] a factor of three or five; The hardware-supported 3-D texture-mapped volume rendering method a factor of about 20. Though 3-D texture-mapped rendering method does not seem to represent in detail information as a ray-casting method does, the image quality of generated DRRs is almost the same as that of high-speed radiographic image and enough to be used for registration between DRRs and radiographic images.

Total processing time for this study was 100 s/frame (two radiographic images), and 3.5 hours for processing the whole sequence (124 motion frames, 248 radiographic images). Manual intervention was required only for determining an initial guess for the first frame of each view (about 5 min). This compares favorably with reported times required to determine 3-D pose of TKA (45 min [18], 15 min [20], or 120 s [19]/frame for both the femoral and tibial component of TKA). In [14], the reason for high performance is that spurious edges were manually identified and deleted, and only a small amount of edge information was used for matching. This approach is not feasible for natural bone tracking.

The largest errors were noted in the X axis rotation of the *in vivo* experiment (corresponding to knee varus/valgus). This result could be predicted, since rotation about this axis appears as motion primarily along the direction of the X-ray beam, and is particularly sensitive to errors in estimated bone size and/or edge location. Accuracy of the other parameters is quite comparable to model-based methods reported for radiographic tracking of TKA component kinematics. Reported *in vitro* errors for 3-D TKA translation range from 0.5 mm to 1.5 mm [13]–[16]. Reported *in vitro* rotational errors are in the order of 1.5° for these TKA studies. From the 3-D model-based method, accuracy for translation and orientation was within 0.5 mm and 1.7° in *in vitro* tests. Given the difference in edge definition between bone and dense metal components, these comparisons are particularly encouraging. These experimental results suggest that this is a promising method to assess bone and joint motion accurately and without the need for implanted radiopaque markers. The method should be applicable for measuring normal and abnormal kinematics of the human knee, and possibly other joints as well.

A limitation of this method is the requirement for a high-resolution CT scan for each subject, to generate 3-D radiographic model of bones to be tracked. Future studies are planned to assess the feasibility of using a library of stored 3-D bone models (possibly scaled to match individual subject anthropometry), which may eliminate the requirement for subject-specific CT scans.

REFERENCES

[1] L. Snyder-Mackler, G. K. Fitzgerald, A. R. Bartolozzi, and M. G. Ciccotti, "The relationship between passive joint laxity and functional outcome after anterior cruciate ligament injure," *Amer. J. Sports Med.*, vol. 25, pp. 191–195, 1997.

[2] M. P. Kadaba, H. K. Ramakrishnan, and M. E. Wootten, "Measurement of lower extremity kinematics during level walking," *J. Orthop. Res.*, vol. 8, pp. 383–392, 1990.

[3] L. -W. Lu and J. J. O'Connor, "Bone position estimation from skin marker coordinates using global optimization with joint constraints," *J. Biomech.*, vol. 32, pp. 129–134, 1999.

[4] A. Capozzo, "Three-dimensional analysis of human walking: experimental methods and associated artifacts," *Human Mov. Sci.*, vol. 10, pp. 589–602, 1991.

[5] L. Lucchitti, A. Cappozzo, A. Cappello, and U. D. Croce, "Skin movement artifact assessment and compensation in the estimation of knee-joint kinematics," *J. Biomech.*, vol. 31, pp. 977–984, 1998.

[6] M. T. G. Pain and J. H. Challis, "Measurement of the soft tissue motion of the thigh during anef39 impact," presented at the North Amer. Congr. Biomech. '98, Waterloo, ON, Canada, Aug. 1998.

[7] J. Fuller, L. -J. Liu, M. C. Murphy, and R. W. Mann, "A comparison of lower-extremity skeletal kinematics measured using skin- and pin-mounted markers," *Human Mov. Sci.*, vol. 16, pp. 219–242, 1997.

[8] M. A. Lafortune, P. R. Cavanagh, H. J. Sommer III, and A. Kalenak, "Three-dimensional kinematics of the human knee during walking," *J. Biomech.*, vol. 25, no. 4, pp. 347–357, 1992.

[9] T. J. Koh, M. D. Grabiner, and R. J. De Swart, "*In vivo* tracking of the human patella," *J. Biomech.*, vol. 25, no. 6, pp. 637–643, 1992.

[10] J. Karrholm, J. Uvehammer, S. Brandson, J. Carlsson, L. Carlsson, L. Regner, and P. Herberts, "*In vivo* kinematics of total knee arthroplasty with flat vs. constrained tibial polyethylene tray," presented at the 44th Annu. Meeting Orthop. Res. Soc., New Orleans, LA, Mar. 1998.

[11] S. Tashman, P. A. Kolowich, T. R. Lock, H. T. Goitz, and E. L. Radin, "Dynamic knee instability following ACL reconstruction in dogs," presented at the 43rdAnnu. Meeting Orthop. Res. Soc., San Francisco, CA, Feb. 1997.

[12] M. Mochimaru and N. Yamazaki, "The marker-less measurement method of the two-dimensional human motion," in *Proc. 10th Conf. Eur. Soc. Biomech.*, Leuven, Belguim, Aug. 1996, p. 290.

[13] H. J. Woltring, P. V. Roy, M. Hebbelinck, M. Osteaux, and L. Verbruggen, "3-D knee joint kinematics by magnetic resonance image," *J. Biomech.*, vol. 23, p. 384, 1990.

[14] W. O. Thompson, F. H. Fu, F. L. Thaete, and S. F. Dye, "Normal meniscal kinematics by three-dimensional reconstructed magnetic resonance images," presented at the Amer. Acad. Orthop. Surgeons 1990 Annu. Meeting—Scientific Program, Sept. 1990.

[15] J. G. Tamez-Pena, S. Totterman, and K. J. Parker, "Kinematic analysis of musculoskeletal structures via volumetric MRI and unsupervised segmentation," presented at the SPIE Med. Imag. '99: Physiology and Function from Multidimensional Images, San Diego, CA, Feb. 1999.

[16] J. Weese, G. P. Penney, P. Desmedt, T. J. Buzug, and D. L. G. Hill, "Voxel-based 2-D/3-D registration of fluoroscopy images and CT scans for image-guided surgery," *IEEE Trans. Infor. Tech. Biomed.*, vol. 1, pp. 248–293, Dec. 1997.

[17] G. P. Penney, J. Weese, J. A. Little, P. Desmedt, D. L. G. Hill, and D. J. Hawkes, "A comparison of similarity measures for use in 2-D-3-D medical image registration," *IEEE Trans. Med. Imag.*, vol. 17, pp. 586–595, Aug. 1998.

[18] S. A. Banks and W. A. Hodge, "Accurate measurement of three-dimensional knee replacement kinematics using single-plane fluoroscopy," *IEEE Trans. Biomed. Eng.*, vol. 44, pp. 638–649, June 1996.

[19] S. Zuffi, A. Leardini, F. Catani, S. Fantozzi, and A. Cappello, "A model-based method for the reconstruction of total knee replacement kinematics," *IEEE Trans. Med. Imag.*, vol. 18, pp. 981–991, Oct. 1999.

[20] M. E. Sarojak, W. A. Hoff, R. D. Komisterk, and D. A. Demis, "Utilization of an automated model fitting process to determine kinematics of TKA," presented at the 23rd Annu. Meeting Amer. Soc. Biomech., Pittsburgh, PA, Oct. 1999.

[21] S. A. Banks, A. Z. Banks, F. F. Cook, and W. A. Hodge, "Markerless three dimensional measurement of knee kinematics using single-plane fluoroscopy," presented at the 20th Annu. Meeting Amer. Soc. Biomech., Atlanta, GE, Oct. 1996.

[22] S. Tashman, K. DuPre, H. Goitz, T. L. Kolowich, and M. Flynn, "A digital radiographic system for determining 3-D joint kinematics during movement," in *Proc. 19th Annu. Meeting Amer. Soc. Biomech.*, Stanford, CA, 1995, pp. 249–250.

[23] D. A. Reimann and M. J. Flynn, "Automated distortion correction of X-ray image intensifier images," in *Proc. IEEE Nuclear Science Symp. Medical Imaging Conf.*, Orlando, FL, 1992, pp. 1339–1341.

[24] S. Tashman, W. Anderst, and P. Kolowich, "Severity of OA related to magnitude of dynamic instability in ACL-deficient dogs," in *Proc. 46th Annu. Meeting Orthop. Res. Soc.*, Orlando, FL, 2000, p. 257.

[25] H. J. Woltring, "Planar control in multi-camera calibration for 3-D gait studies," *J. Biomech.*, vol. 33, pp. 39–44, 1980.

[26] A. Kaufan, *Volume Visualization*. Los Alamitos, CA: IEEE Comput. Soc. Press, 1991.

[27] W. Schroeder, K. Martin, and B. Lorensen, *The Visualization Toolkit: An Object-Oriented Approach to 3-D Graphics*. Englewood Cliffs, NJ: Prentice-Hall, 1996.

[28] F. F. Yin, Q. Gao, H. Xie, D. F. Nelson, Y. Yu, W. E. Kwok, S. Totterman, M. C. Schell, and P. Rubin, "MR image-guided portal verification for brain treatment field," *Int. J. Radiat. Oncol., Biol., Phys.*, vol. 40, no. 3, pp. 703–711, 1998.

[29] L. Lemieux, R. Jagoe, D. R. Fish, N. D. Kitchen, and D. G. T. Thomas, "A patient-to-computed-tomography image registration method based on digitally reconstructed radiographs," *Amer. Assoc. Med. Phys*, vol. 21, no. 11, pp. 1749–1760, 1994.

[30] R. A. Drebin, L. Carpenter, and P. Hanrahan, "Volume rendering," *Comput. Graph.*, vol. 22, no. 4, pp. 65–74, Aug. 1988.

[31] J. Weese, R. Gocke, and G. P. Penney, "Fast voxel-based 2-D/3-D registration algorithm using a volume rendering method based on the shear-warp factorization," in *Proc. SPIE Med. Imag. '99 Image Processing*, vol. 3979, San Diego, CA, Feb. 2000, pp. 385–396.

[32] D. LaRose, J. Bayouth, and T. Kanade, "Transgraph: interactive intensity-based 2-D/3-D registration of X-ray and CT data," in *Proc. SPIE Med. Imag. '2000 Image Processing*, vol. 3979, San Diego, CA, Feb. 2000, pp. 385–396.

[33] J. Neider, T. Davis, and M. Woo, *OpenGL Programming Guide*. Reading, MA: Addison-Wesley, 1998.

[34] R. J. Schalkoff, *Digital Image Processing and Computer Vision*. New York: Wiley, 1989.

[35] M. Sonka, V. Hlavac, and R. Boyle, *Image Processing, Analysis and Machine Vision*. London, U.K.: Champan & Hall, 1995.

[36] W. H. Press, S. A. Teukolsky, W. T. Vetterling, and B. T. Flannery, *Numerical Recipes in C: The Art of Scientific Computing*, 2 ed, NY: Cambridge Univ. Press, 1988.

[37] D. A. Pierre, *Optimization Theory with Application*. New York: Dover, 1986.

[38] W. J. Suntay, E. S. Grood, M. S. Hefzy, D. L. Butler, and F. R. Noyes, "Error analysis of a system for measuring three-dimensional joint motion," *J. Biomech. Eng.*, vol. 105, pp. 127–135, 1983.

[39] P. Bourke. The shortest line between two lines in 3-D. [Online]. Available: http://www.swin.edu.au/astronomy/pborke/geometry/lineline3d/

[40] J. J. Craig, *Introduction to Robotics Mechanics & Control*. Reading, MA: Addison-Welsey, 1995.

[41] T. R. Kane, P. W. Likins, and D. A. Levinson, *Spacecraft Dynamics*. New York: McGraw-Hill, 1983.